Title
Dalitz plot analysis of B-→D+π-π-

Authors
Aubert, B
Bona, M
Karyotakis, Y
et al.

Dalitz plot analysis of $B^- \rightarrow D^+ \pi^- \pi^-$

B. Aubert,[1] M. Bona,[1] Y. Karyotakis,[1] J. P. Lees,[1] V. Poireau,[1] E. Prencipe,[1] X. Prudent,[1] V. Tisserand,[1] J. Garra Tico,[2] E. Grauges,[2] L. Lopez,[3a,3b] A. Palano,[3a,3b] M. Pappagallo,[3a,3b] G. Eigen,[4] B. Stugu,[4] L. Sun,[4] G. S. Abrams,[5] M. Battaglia,[5] D. N. Brown,[5] R. G. Jacobsen,[5] L. T. Kerth,[5] Yu. G. Kolomensky,[5] G. Lynch,[5] I. L. Osipenkov,[5] M. T. Ronan,[5,*] K. Tackmann,[5] T. Tanabe,[5] C. M. Hawkes,[6] N. Soni,[6] A. T. Watson,[6] H. Koch,[7] T. Schroeder,[7] D. J. Asgeirsson,[8] B. G. Fulsom,[8] C. Hearty,[8] T. S. Mattison,[8] J. A. McKenna,[8] M. Barrett,[9] A. Khan,[9] V. E. Blinov,[10] A. D. Bukin,[10] A. R. Buzykaev,[10] V. P. Druzhinin,[10] V. B. Golubev,[10] A. P. Onuchin,[10] S. I. Serednyakov,[10] Yu. I. Skovpen,[10] E. P. Solodov,[10] K. Yu. Todyshev,[10] M. Bondioli,[11] S. Curry,[11] I. Eschrich,[11] D. Kirkby,[11] A. J. Lankford,[11] P. Lund,[11] M. Mandelkern,[11] E. C. Martin,[11] D. P. Stoker,[11] S. Abachi,[12] C. Buchanan,[12] H. Atmacan,[13] J. W. Gary,[13] F. Liu,[13] O. Long,[13] G. M. Vitug,[13] Z. Yasin,[13] L. Zhang,[13] V. Sharma,[14] C. Campagnari,[15] T. M. Hong,[15] D. Kovalskyi,[15] M. A. Mazur,[15] J. D. Richman,[15] T. W. Beck,[16] A. M. Eisner,[16] C. J. Flacco,[16] C. A. Heusch,[16] J. Kroseberg,[16] W. S. Lockman,[16] A. J. Martinez,[16] T. Schalk,[16] B. A. Schumm,[16] A. Seiden,[16] M. G. Wilson,[16] L. O. Winstrom,[16] C. H. Cheng,[17] D. A. Doll,[17] B. Echenard,[17] F. Fang,[17] D. G. Hitlin,[17] I. Narsky,[17] T. Piatenko,[17] F. C. Porter,[17] R. Andreassen,[18] G. Mancinelli,[18] B. T. Meadows,[18] K. Mishra,[18] M. D. Sokoloff,[18] P. C. Bloom,[19] W. T. Ford,[19] A. Gaz,[19] J. F. Hirschauer,[19] M. Nagel,[19] U. Nauenberg,[19] J. G. Smith,[19] S. R. Wagner,[19] R. Ayad,[20,†] A. Soffer,[20,‡] W. H. Toki,[20] R. J. Wilson,[20] E. Feltresi,[21] A. Hauke,[21] H. Jasper,[21] M. Karbach,[21] J. Merkel,[21] A. Petzold,[21] B. Spaan,[21] K. Wacker,[21] M. J. Kobel,[22] R. Nogowski,[22] K. R. Schubert,[22] R. Schwierz,[22] A. Volk,[22] D. Bernard,[23] G. R. Bonneaud,[23] E. Latour,[23] M. Verderi,[23] P. J. Clark,[24] S. Playfer,[24] J. E. Watson,[24] M. Andreotti,[25a,25b] D. Bettoni,[25a] C. Bozzi,[25a] R. Calabrese,[25a,25b] A. Cecchi,[25a,25b] G. Cibinetto,[25a,25b] P. Franchini,[25a,25b] E. Luppi,[25a,25b] M. Negrini,[25a,25b] A. Petrella,[25a,25b] L. Piemontese,[25a] V. Santoro,[25a,25b] R. Baldini-Ferroli,[26] A. Calcaterra,[26] R. de Sangro,[26] G. Finocchiaro,[26] S. Pacetti,[26] P. Patteri,[26] I. M. Peruzzi,[26,§] M. Piccolo,[26] M. Rama,[26] A. Zallo,[26] A. Buzzo,[27a] R. Contri,[27a,27b] M. Lo Vetere,[27a,27b] M. M. Macri,[27a] M. R. Monge,[27a,27b] S. Passaggio,[27a] C. Patrignani,[27a,27b] E. Robutti,[27a] A. Santroni,[27a,27b] S. Tosi,[27a,27b] K. S. Chaisanguanthum,[28] M. Morii,[28] A. Adametz,[29] J. Marks,[29] S. Schenk,[29] U. Uwer,[29] V. Klose,[30] H. M. Lacker,[30] D. J. Bard,[31] P. D. Dauncey,[31] M. Tibbetts,[31] P. K. Behera,[32] X. Chai,[32] M. J. Charles,[32] U. Mallik,[32] J. Cochran,[33] H. B. Crawley,[33] L. Dong,[33] W. T. Meyer,[33] S. Prell,[33] E. I. Rosenberg,[33] A. E. Rubin,[33] Y. Y. Gao,[34] A. V. Gritsan,[34] Z. J. Guo,[34] C. K. Lae,[34] N. Arnaud,[35] J. Béquilleux,[35] A. D'Orazio,[35] M. Davier,[35] J. Firmino da Costa,[35] G. Grosdidier,[35] F. Le Diberder,[35] V. Lepeltier,[35] A. M. Lutz,[35] S. Pruvot,[35] P. Roudeau,[35] M. H. Schune,[35] J. Serrano,[35] V. Sordini,[35,‖] A. Stocchi,[35] G. Wormser,[35] D. J. Lange,[36] D. M. Wright,[36] I. Bingham,[37] J. P. Burke,[37] C. A. Chavez,[37] J. R. Fry,[37] E. Gabathuler,[37] R. Gamet,[37] D. E. Hutchcroft,[37] D. J. Payne,[37] C. Touramanis,[37] A. J. Bevan,[38] C. K. Clarke,[38] F. Di Lodovico,[38] R. Sacco,[38] M. Sigamani,[38] G. Cowan,[39] S. Paramesvaran,[39] A. C. Wren,[39] D. N. Brown,[40] C. L. Davis,[40] A. G. Denig,[41] M. Fritsch,[41] W. Gradl,[41] K. E. Alwyn,[42] D. Bailey,[42] R. J. Barlow,[42] G. Jackson,[42] G. D. Lafferty,[42] T. J. West,[42] J. I. Yi,[42] J. Anderson,[43] C. Chen,[43] A. Jawahery,[43] D. A. Roberts,[43] G. Simi,[43] J. M. Tuggle,[43] C. Dallapiccola,[44] X. Li,[44] E. Salvati,[44] S. Saremi,[44] R. Cowan,[45] D. Dujmic,[45] P. H. Fisher,[45] S. W. Henderson,[45] G. Sciolla,[45] M. Spitznagel,[45] F. Taylor,[45] R. K. Yamamoto,[45] M. Zhao,[45] P. M. Patel,[46] S. H. Robertson,[46] A. Lazzaro,[47a,47b] V. Lombardo,[47a] F. Palombo,[47a,47b] J. M. Bauer,[48] L. Cremaldi,[48] R. Godang,[48,¶] R. Kroeger,[48] D. J. Summers,[48] H. W. Zhao,[48] M. Simard,[49] P. Taras,[49] H. Nicholson,[50] G. De Nardo,[51a,51b] L. Lista,[51a] D. Monorchio,[51a,51b] G. Onorato,[51a,51b] C. Sciacca,[51a,51b] G. Raven,[52] H. L. Snoek,[52] C. P. Jessop,[53] K. J. Knoepfel,[53] J. M. LoSecco,[53] W. F. Wang,[53] L. A. Corwin,[54] K. Honscheid,[54] H. Kagan,[54] R. Kass,[54] J. P. Morris,[54] A. M. Rahimi,[54] J. J. Regensburger,[54] S. J. Sekula,[54] Q. K. Wong,[54] N. L. Blount,[55] J. Brau,[55] R. Frey,[55] O. Igonkina,[55] J. A. Kolb,[55] M. Lu,[55] R. Rahmat,[55] N. B. Sinev,[55] D. Strom,[55] J. Strube,[55] E. Torrence,[55] G. Castelli,[56a,56b] N. Gagliardi,[56a,56b] M. Margoni,[56a,56b] M. Morandin,[56a] M. Posocco,[56a] M. Rotondo,[56a] F. Simonetto,[56a,56b] R. Stroili,[56a,56b] C. Voci,[56a,56b] P. del Amo Sanchez,[57] E. Ben-Haim,[57] H. Briand,[57] G. Calderini,[57] J. Chauveau,[57] O. Hamon,[57] Ph. Leruste,[57] J. Ocariz,[57] A. Perez,[57] J. Prendki,[57] S. Sitt,[57] L. Gladney,[58] M. Biasini,[59a,59b] E. Manoni,[59a,59b] C. Angelini,[60a,60b] G. Batignani,[60a,60b] S. Bettarini,[60a,60b] M. Carpinelli,[60a,60b,**] A. Cervelli,[60a,60b] F. Forti,[60a,60b] M. A. Giorgi,[60a,60b] A. Lusiani,[60a,60c] G. Marchiori,[60a,60b] M. Morganti,[60a,60b] N. Neri,[60a,60b] E. Paoloni,[60a,60b] G. Rizzo,[60a,60b] J. J. Walsh,[60a] D. Lopes Pegna,[61] C. Lu,[61] J. Olsen,[61] A. J. S. Smith,[61] A. V. Telnov,[61] F. Anulli,[61] E. Baracchini,[62a,62b] G. Cavoto,[62a] R. Faccini,[62a,62b] F. Ferrarotto,[62a] F. Ferroni,[62a,62b] M. Gaspero,[62a,62b] P. D. Jackson,[62a] L. Li Gioi,[62a] M. A. Mazzoni,[62a] S. Morganti,[62a] G. Piredda,[62a] F. Renga,[62a,62b] C. Voena,[62a] M. Ebert,[63] T. Hartmann,[63] H. Schröder,[63] R. Waldi,[63] T. Adye,[64] B. Franek,[64] E. O. Olaiya,[64] F. F. Wilson,[64] S. Emery,[65] M. Escalier,[65] L. Esteve,[65] G. Hamel de Monchenault,[65] W. Kozanecki,[65] G. Vasseur,[65] Ch. Yèche,[65] M. Zito,[65] X. R. Chen,[66] H. Liu,[66] W. Park,[66] M. V. Purohit,[66] R. M. White,[66] J. R. Wilson,[66]

M. T. Allen,[67] D. Aston,[67] R. Bartoldus,[67] J. F. Benitez,[67] R. Cenci,[67] J. P. Coleman,[67] M. R. Convery,[67] J. C. Dingfelder,[67] J. Dorfan,[67] G. P. Dubois-Felsmann,[67] W. Dunwoodie,[67] R. C. Field,[67] A. M. Gabareen,[67] M. T. Graham,[67] P. Grenier,[67] C. Hast,[67] W. R. Innes,[67] J. Kaminski,[67] M. H. Kelsey,[67] H. Kim,[67] P. Kim,[67] M. L. Kocian,[67] D. W. G. S. Leith,[67] S. Li,[67] B. Lindquist,[67] S. Luitz,[67] V. Luth,[67] H. L. Lynch,[67] D. B. MacFarlane,[67] H. Marsiske,[67] R. Messner,[67] D. R. Muller,[67] H. Neal,[67] S. Nelson,[67] C. P. O'Grady,[67] I. Ofte,[67] M. Perl,[67] B. N. Ratcliff,[67] A. Roodman,[67] A. A. Salnikov,[67] R. H. Schindler,[67] J. Schwiening,[67] A. Snyder,[67] D. Su,[67] M. K. Sullivan,[67] K. Suzuki,[67] S. K. Swain,[67] J. M. Thompson,[67] J. Va'vra,[67] A. P. Wagner,[67] M. Weaver,[67] C. A. West,[67] W. J. Wisniewski,[67] M. Wittgen,[67] D. H. Wright,[67] H. W. Wulsin,[67] A. K. Yarritu,[67] K. Yi,[67] C. C. Young,[67] V. Ziegler,[67] P. R. Burchat,[68] A. J. Edwards,[68] T. S. Miyashita,[68] S. Ahmed,[69] M. S. Alam,[69] J. A. Ernst,[69] B. Pan,[69] M. A. Saeed,[69] S. B. Zain,[69] S. M. Spanier,[70] B. J. Wogsland,[70] R. Eckmann,[71] J. L. Ritchie,[71] A. M. Ruland,[71] C. J. Schilling,[71] R. F. Schwitters,[71] B. W. Drummond,[72] J. M. Izen,[72] X. C. Lou,[72] F. Bianchi,[73a,73b] D. Gamba,[73a,73b] M. Pelliccioni,[73a,73b] M. Bomben,[74a,74b] L. Bosisio,[74a,74b] C. Cartaro,[74a,74b] G. Della Ricca,[74a,74b] L. Lanceri,[74a,74b] L. Vitale,[74a,74b] V. Azzolini,[75] N. Lopez-March,[75] F. Martinez-Vidal,[75] D. A. Milanes,[75] A. Oyanguren,[75] J. Albert,[76] Sw. Banerjee,[76] B. Bhuyan,[76] H. H. F. Choi,[76] K. Hamano,[76] R. Kowalewski,[76] M. J. Lewczuk,[76] I. M. Nugent,[76] J. M. Roney,[76] R. J. Sobie,[76] T. J. Gershon,[77] P. F. Harrison,[77] J. Ilic,[77] T. E. Latham,[77] G. B. Mohanty,[77] H. R. Band,[78] X. Chen,[78] S. Dasu,[78] K. T. Flood,[78] Y. Pan,[78] R. Prepost,[78] C. O. Vuosalo,[78] and S. L. Wu[78]

(*BABAR* Collaboration)

[1]*Laboratoire de Physique des Particules, IN2P3/CNRS et Université de Savoie, F-74941 Annecy-Le-Vieux, France*
[2]*Universitat de Barcelona, Facultat de Fisica, Departament ECM, E-08028 Barcelona, Spain*
[3a]*INFN Sezione di Bari, I-70126 Bari, Italy*
[3b]*Dipartimento di Fisica, Università di Bari, I-70126 Bari, Italy*
[4]*University of Bergen, Institute of Physics, N-5007 Bergen, Norway*
[5]*Lawrence Berkeley National Laboratory and University of California, Berkeley, California 94720, USA*
[6]*University of Birmingham, Birmingham, B15 2TT, United Kingdom*
[7]*Ruhr Universität Bochum, Institut für Experimentalphysik 1, D-44780 Bochum, Germany*
[8]*University of British Columbia, Vancouver, British Columbia, Canada V6T 1Z1*
[9]*Brunel University, Uxbridge, Middlesex UB8 3PH, United Kingdom*
[10]*Budker Institute of Nuclear Physics, Novosibirsk 630090, Russia*
[11]*University of California at Irvine, Irvine, California 92697, USA*
[12]*University of California at Los Angeles, Los Angeles, California 90024, USA*
[13]*University of California at Riverside, Riverside, California 92521, USA*
[14]*University of California at San Diego, La Jolla, California 92093, USA*
[15]*University of California at Santa Barbara, Santa Barbara, California 93106, USA*
[16]*University of California at Santa Cruz, Institute for Particle Physics, Santa Cruz, California 95064, USA*
[17]*California Institute of Technology, Pasadena, California 91125, USA*
[18]*University of Cincinnati, Cincinnati, Ohio 45221, USA*
[19]*University of Colorado, Boulder, Colorado 80309, USA*
[20]*Colorado State University, Fort Collins, Colorado 80523, USA*
[21]*Technische Universität Dortmund, Fakultät Physik, D-44221 Dortmund, Germany*
[22]*Technische Universität Dresden, Institut für Kern- und Teilchenphysik, D-01062 Dresden, Germany*
[23]*Laboratoire Leprince-Ringuet, CNRS/IN2P3, Ecole Polytechnique, F-91128 Palaiseau, France*
[24]*University of Edinburgh, Edinburgh EH9 3JZ, United Kingdom*
[25a]*INFN Sezione di Ferrara, I-44100 Ferrara, Italy*
[25b]*Dipartimento di Fisica, Università di Ferrara, I-44100 Ferrara, Italy*
[26]*INFN Laboratori Nazionali di Frascati, I-00044 Frascati, Italy*
[27a]*INFN Sezione di Genova, I-16146 Genova, Italy*
[27b]*Dipartimento di Fisica, Università di Genova, I-16146 Genova, Italy*
[28]*Harvard University, Cambridge, Massachusetts 02138, USA*
[29]*Universität Heidelberg, Physikalisches Institut, Philosophenweg 12, D-69120 Heidelberg, Germany*
[30]*Humboldt-Universität zu Berlin, Institut für Physik, Newtonstr. 15, D-12489 Berlin, Germany*
[31]*Imperial College London, London, SW7 2AZ, United Kingdom*
[32]*University of Iowa, Iowa City, Iowa 52242, USA*
[33]*Iowa State University, Ames, Iowa 50011-3160, USA*
[34]*Johns Hopkins University, Baltimore, Maryland 21218, USA*

[35]*Laboratoire de l'Accélérateur Linéaire, IN2P3/CNRS et Université Paris-Sud 11,*
Centre Scientifique d'Orsay, B. P. 34, F-91898 Orsay Cedex, France
[36]*Lawrence Livermore National Laboratory, Livermore, California 94550, USA*
[37]*University of Liverpool, Liverpool L69 7ZE, United Kingdom*
[38]*Queen Mary, University of London, London, E1 4NS, United Kingdom*
[39]*University of London, Royal Holloway and Bedford New College, Egham, Surrey TW20 0EX, United Kingdom*
[40]*University of Louisville, Louisville, Kentucky 40292, USA*
[41]*Johannes Gutenberg-Universität Mainz, Institut für Kernphysik, D-55099 Mainz, Germany*
[42]*University of Manchester, Manchester M13 9PL, United Kingdom*
[43]*University of Maryland, College Park, Maryland 20742, USA*
[44]*University of Massachusetts, Amherst, Massachusetts 01003, USA*
[45]*Massachusetts Institute of Technology, Laboratory for Nuclear Science, Cambridge, Massachusetts 02139, USA*
[46]*McGill University, Montréal, Québec, Canada H3A 2T8*
[47a]*INFN Sezione di Milano, I-20133 Milano, Italy*
[47b]*Dipartimento di Fisica, Università di Milano, I-20133 Milano, Italy*
[48]*University of Mississippi, University, Mississippi 38677, USA*
[49]*Université de Montréal, Physique des Particules, Montréal, Québec, Canada H3C 3J7*
[50]*Mount Holyoke College, South Hadley, Massachusetts 01075, USA*
[51a]*INFN Sezione di Napoli, I-80126 Napoli, Italy*
[51b]*Dipartimento di Scienze Fisiche, Università di Napoli Federico II, I-80126 Napoli, Italy*
[52]*NIKHEF, National Institute for Nuclear Physics and High Energy Physics, NL-1009 DB Amsterdam, The Netherlands*
[53]*University of Notre Dame, Notre Dame, Indiana 46556, USA*
[54]*Ohio State University, Columbus, Ohio 43210, USA*
[55]*University of Oregon, Eugene, Oregon 97403, USA*
[56a]*INFN Sezione di Padova, I-35131 Padova, Italy*
[56b]*Dipartimento di Fisica, Università di Padova, I-35131 Padova, Italy*
[57]*Laboratoire de Physique Nucléaire et de Hautes Energies, IN2P3/CNRS, Université Pierre et Marie Curie-Paris6,*
Université Denis Diderot-Paris7, F-75252 Paris, France
[58]*University of Pennsylvania, Philadelphia, Pennsylvania 19104, USA*
[59a]*INFN Sezione di Perugia, I-06100 Perugia, Italy*
[59b]*Dipartimento di Fisica, Università di Perugia, I-06100 Perugia, Italy*
[60a]*INFN Sezione di Pisa, I-56127 Pisa, Italy*
[60b]*Dipartimento di Fisica, Università di Pisa, I-56127 Pisa, Italy*
[60c]*Scuola Normale Superiore di Pisa, I-56127 Pisa, Italy*
[61]*Princeton University, Princeton, New Jersey 08544, USA*
[62a]*INFN Sezione di Roma, I-00185 Roma, Italy*
[62b]*Dipartimento di Fisica, Università di Roma La Sapienza, I-00185 Roma, Italy*
[63]*Universität Rostock, D-18051 Rostock, Germany*
[64]*Rutherford Appleton Laboratory, Chilton, Didcot, Oxon, OX11 0QX, United Kingdom*
[65]*CEA, Irfu, SPP, Centre de Saclay, F-91191 Gif-sur-Yvette, France*
[66]*University of South Carolina, Columbia, South Carolina 29208, USA*
[67]*Stanford Linear Accelerator Center, Stanford, California 94309, USA*
[68]*Stanford University, Stanford, California 94305-4060, USA*
[69]*State University of New York, Albany, New York 12222, USA*
[70]*University of Tennessee, Knoxville, Tennessee 37996, USA*
[71]*University of Texas at Austin, Austin, Texas 78712, USA*
[72]*University of Texas at Dallas, Richardson, Texas 75083, USA*
[73a]*INFN Sezione di Torino, I-10125 Torino, Italy*
[73b]*Dipartimento di Fisica Sperimentale, Università di Torino, I-10125 Torino, Italy*
[74a]*INFN Sezione di Trieste, I-34127 Trieste, Italy*
[74b]*Dipartimento di Fisica, Università di Trieste, I-34127 Trieste, Italy*
[75]*IFIC, Universitat de Valencia-CSIC, E-46071 Valencia, Spain*
[76]*University of Victoria, Victoria, British Columbia, Canada V8W 3P6*

[*]Deceased.
[†]Now at Temple University, Philadelphia, PA 19122, USA.
[‡]Now at Tel Aviv University, Tel Aviv, 69978, Israel.
[§]Also with Università di Perugia, Dipartimento di Fisica, Perugia, Italy.
[‖]Also with Università di Roma La Sapienza, I-00185 Roma, Italy.
[¶]Now at University of South Alabama, Mobile, AL 36688, USA.
[**]Also with Università di Sassari, Sassari, Italy.

[77]*Department of Physics, University of Warwick, Coventry CV4 7AL, United Kingdom*
[78]*University of Wisconsin, Madison, Wisconsin 53706, USA*

We report on a Dalitz plot analysis of $B^- \to D^+\pi^-\pi^-$ decays, based on a sample of about 383×10^6 $\Upsilon(4S) \to B\bar{B}$ decays collected with the *BABAR* detector at the PEP-II asymmetric-energy *B* Factory at SLAC. We find the total branching fraction of the three-body decay: $\mathcal{B}(B^- \to D^+\pi^-\pi^-) = (1.08 \pm 0.03 \pm 0.05) \times 10^{-3}$. We observe the established D_2^{*0} and confirm the existence of D_0^{*0} in their decays to $D^+\pi^-$, where the D_2^{*0} and D_0^{*0} are the 2^+ and 0^+ $c\bar{u}$ *P*-wave states, respectively. We measure the masses and widths of D_2^{*0} and D_0^{*0} to be: $m_{D^{*0}_2} = (2460.4 \pm 1.2 \pm 1.2 \pm 1.9)$ MeV/c^2, $\Gamma_{D^{*0}_2} = (41.8 \pm 2.5 \pm 2.1 \pm 2.0)$ MeV, $m_{D^{*0}_0} = (2297 \pm 8 \pm 5 \pm 19)$ MeV/c^2, and $\Gamma_{D^{*0}_0} = (273 \pm 12 \pm 17 \pm 45)$ MeV. The stated errors reflect the statistical and systematic uncertainties, and the uncertainty related to the assumed composition of signal events and the theoretical model.

I. INTRODUCTION

Orbitally excited states of the *D* meson, denoted here as D_J, where *J* is the spin of the meson, provide a unique opportunity to test the heavy quark effective theory (HQET) [1,2]. The simplest D_J meson consists of a charm quark and a light antiquark in an orbital angular momentum $L = 1$ (*P*-wave) state. Four such states are expected with spin-parity 0^+ ($j = 1/2$), 1^+ ($j = 1/2$), 1^+ ($j = 3/2$), and 2^+ ($j = 3/2$), which are labeled here as D_0^*, D_1', D_1, and D_2^*, respectively, where *j* is a quantum number corresponding to the sum of the light quark spin and the orbital angular momentum $\vec{L}$.

The conservation of parity and angular momentum in strong interactions imposes constraints on the strong decays of D_J states to $D\pi$ and $D^*\pi$. The $j = 1/2$ states are predicted to decay exclusively through an *S*-wave: $D_0^* \to D\pi$ and $D_1' \to D^*\pi$. The $j = 3/2$ states are expected to decay through a *D*-wave: $D_1 \to D^*\pi$ and $D_2^* \to D\pi$ and $D^*\pi$. These transitions are summarized in Fig. 1. Because
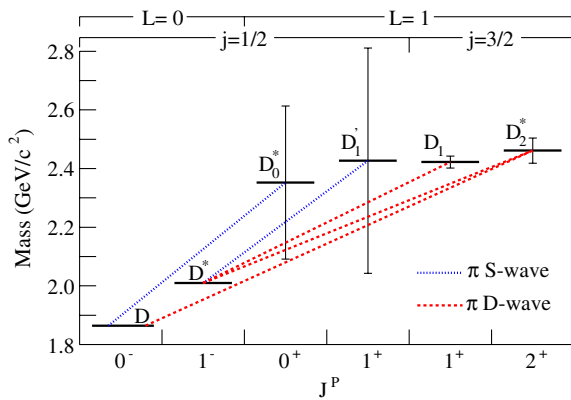
FIG. 1 (color online). Mass spectrum for $c\bar{u}$ states. The vertical bars show the widths. Masses and widths are from Ref. [5]. The dotted and dashed lines between the levels show the dominant pion transitions. Although it is not indicated in the figure, the two 1^+ states may be mixtures of $j = 1/2$ and $j = 3/2$, and D_1' may decay via a *D*-wave and D_1 may decay via an *S*-wave.

of the finite *c*-quark mass, the two $J^P = 1^+$ states may be mixtures of the $j = 1/2$ and $j = 3/2$ states. Thus the broad D_1' state may decay via a *D*-wave and the narrow D_1 state may decay via an *S*-wave. The $j = 1/2$ states with $L = 1$, which decay through an *S*-wave, are expected to be wide (hundreds of MeV/c^2), while the $j = 3/2$ states that decay through a *D*-wave are expected to be narrow (tens of MeV/c^2) [2–4]. Properties of the $L = 1$ D_J^0 mesons [5] are given in Table I.

The narrow D_J mesons have been previously observed and studied by a number of experiments [6–16]. D_J mesons have also been studied in semileptonic *B* decays [17–24]. Precise knowledge of the properties of the D_J mesons is important to reduce uncertainties in the measurements of semileptonic decays, and thus the determination of the Cabibbo-Kobayashi-Maskawa [25] matrix elements $|V_{cb}|$ and $|V_{ub}|$. The Belle Collaboration has reported the first observation of the broad D_0^{*0} and $D_1'^0$ mesons in *B* decay [12]. The FOCUS Collaboration has found evidence for broad structures in $D^+\pi^-$ final states [13] with mass and width in agreement with the D_0^{*0} found by the Belle Collaboration. However, the Particle Data Group [5] considers that the *J* and *P* quantum numbers of the D_0^{*0} and $D_1'^0$ states still need confirmation.

In this analysis, we fully reconstruct the decays $B^- \to D^+\pi^-\pi^-$ [26] and measure their branching fraction. We also perform an analysis of the Dalitz plot (DP) to measure the exclusive branching fractions of $B^- \to D_J^0\pi^-$ and study the properties of the D_J^0 mesons. The decay $B^- \to D^+\pi^-\pi^-$ is expected to be dominated by the intermediate

TABLE I. Properties of $L = 1$ D_J^0 mesons [5].

	J^P	Mass (MeV/c^2)	Width (MeV)	Decays seen [5]	Partial waves
D_0^{*0}	0^+	2352 ± 50	261 ± 50	$D\pi$	S
$D_1'^0$	1^+	2427 ± 36	384^{+130}_{-105}	$D^*\pi$	S, D
D_1^0	1^+	2422.3 ± 1.3	20.4 ± 1.7	$D^*\pi, D^0\pi^+\pi^-$	S, D
D_2^{*0}	2^+	2461.1 ± 1.6	43 ± 4	$D^*\pi, D\pi$	D

states $D_2^{*0}\pi^-$ and $D_0^{*0}\pi^-$ and has a possible contribution from $B^- \to D^+\pi^-\pi^-$ nonresonant (NR) decay. The D_1^0 and $D_1'^0$ states cannot decay strongly into $D\pi$ because of parity and angular momentum conservation. However, the $D^*(2007)^0$ (labeled as D_v^* here) mass is close to the $D\pi$ production threshold and it may contribute as a virtual intermediate state. The B^* (labeled as B_v^* here) produced in a virtual process $B^- \to B_v^*\pi^-$ may also contribute via the decay $B_v^* \to D^+\pi^-$. Possible contributions from these virtual states are also studied in this analysis.

II. THE *BABAR* DETECTOR AND DATA SET

The data used in this analysis were collected with the *BABAR* detector at the PEP-II asymmetric-energy e^+e^- storage rings at SLAC between 1999 and 2006. The sample consists of 347.2 fb^{-1} corresponding to $(382.9 \pm 4.2) \times 10^6$ $B\bar{B}$ pairs ($N_{B\bar{B}}$) taken on the peak of the $\Upsilon(4S)$ resonance. Monte Carlo (MC) simulation is used to study the detector response, its acceptance, background, and to validate the analysis. We use GEANT4 [27] to simulate resonant $e^+e^- \to \Upsilon(4S) \to B\bar{B}$ events (generated by EvtGen [28]) and $e^+e^- \to q\bar{q}$ (where $q = u$, d, s, or c) continuum events (generated by JETSET [29]).

A detailed description of the *BABAR* detector is given in Ref. [30]. Charged particle trajectories are measured by a five-layer, double-sided silicon vertex tracker (SVT) and a 40-layer drift chamber (DCH) immersed in a 1.5 T magnetic field. Charged particle identification (PID) is achieved by combining information from a ring-imaging Cherenkov device with ionization energy loss (dE/dx) measurements in the DCH and SVT.

III. EVENT SELECTION

Five charged particles are selected to reconstruct decays of $B^- \to D^+\pi^-\pi^-$ with $D^+ \to K^-\pi^+\pi^+$. The charged particle candidates are required to have transverse momenta above 100 MeV/c and at least 12 hits in the DCH. A K^- candidate must be identified as a kaon using a likelihood-based particle identification algorithm (with an average efficiency of ~85% and an average misidentification probability of ~3%). Any combination of $K^-\pi^+\pi^+$ candidates with a common vertex and an invariant mass between 1.8625 and 1.8745 GeV/c^2 is accepted as a D^+ candidate. We fit the invariant mass distribution of the $K^-\pi^+\pi^+$ candidates with a function that includes a Gaussian component for the signal and a linear term for the background. The signal parameters (mean and width of Gaussian) and slope of the background function are free parameters of the fit. The data and the result of the fit are shown in Fig. 2. The invariant mass resolution for this D^+ decay is about 5.2 MeV/c^2. The B^- candidates are reconstructed by combining a D^+ candidate and two charged tracks. The trajectories of the three daughters of the B^- meson candidate are constrained to originate from a com-
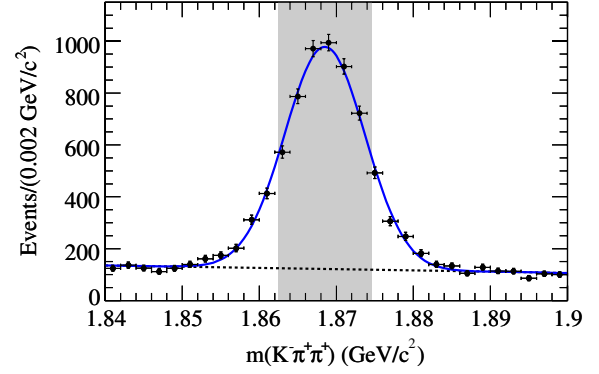
FIG. 2 (color online). $K^+\pi^-\pi^-$ invariant mass distribution for D^+ candidates for the selected $B^- \to D^+\pi^-\pi^-$ decays without the cut on the mass of D^+. Data (points with statistical errors) are compared to the results of the fit (solid curve), with the background distribution marked as a dashed line. The shaded area marks the D^+ signal region.

mon decay vertex. The D^+ and B^- vertex fits are required to have converged.

At the $\Upsilon(4S)$ resonance, B mesons can be characterized by two nearly independent kinematic variables, the beam-energy substituted mass m_{ES} and the energy difference ΔE:

$$m_{ES} = \sqrt{(s/2 + \vec{p}_0 \cdot \vec{p}_B)^2/E_0^2 - p_B^2}, \tag{1}$$

$$\Delta E = E_B^* - \sqrt{s}/2, \tag{2}$$

where E and p are energy and momentum, the subscripts 0 and B refer to the e^+e^--beam system and the B candidate, respectively; s is the square of the center-of-mass energy and the asterisk labels the center-of-mass frame. For $B^- \to D^+\pi^-\pi^-$ signal events, the m_{ES} distribution is well described by a Gaussian resolution function with a width of 2.6 MeV/c^2 centered at the B^- meson mass, while the ΔE distribution can be represented by a sum of two Gaussian functions with a common mean near zero and different widths with a combined root-mean-square (RMS) of 20 MeV.

Continuum events are the dominant background. Suppression of background from continuum events is provided by two topological requirements. In particular, we employ restrictions on the magnitude of the cosine of the thrust angle, $\cos\Theta_{th}$, defined as the angle between the thrust axis of the selected B candidate and the thrust axis of the remaining tracks and neutral clusters in the event. The distribution of $|\cos\Theta_{th}|$ is strongly peaked towards unity for continuum background but is uniform for signal events. We also select on the ratio of the second to the zeroth Fox-Wolfram moment [31], R_2, to further reduce the continuum background. The value of R_2 ranges from 0 to 1. Small values of R_2 indicate a more spherical event shape (typical for a $B\bar{B}$ event) while values close to 1 indicate a 2-jet event topology (typical for a $q\bar{q}$ event). We accept the

events with $|\cos\Theta_{\text{th}}| < 0.85$ and $R_2 < 0.30$. The $|\cos\Theta_{\text{th}}|$ (R_2) cut eliminates about 68% (71%) of the continuum background while retaining about 90% (83%) of signal events.

To suppress backgrounds, restrictions are placed on m_{ES}: $5.2754 < m_{\text{ES}} < 5.2820$ GeV/c^2, and ΔE: $-130 < \Delta E < 130$ MeV. The selected samples of B candidates are used as input to an unbinned extended maximum likelihood fit to the ΔE distribution. The result of the fit is used to determine the fractions of signal and background events in the selected data sample. For events with multiple candidates ($\sim 3.5\%$ of the selected events) satisfying the selection criteria, we choose the one with best χ^2 from the B vertex fit. Based on MC simulation, we determine that the correct candidate is selected at least 65% of the time. We fit the m_{ES} distribution of the selected $B^- \to D^+\pi^-\pi^-$ candidates with a sum of a Gaussian function for the signal and a background function for the background having the probability density, $P(x) \propto x\sqrt{1-x^2}\exp(-\xi(1-x^2))$, where $x = m_{\text{ES}}/m_0$ with m_0 fixed at 5.29 GeV/c^2 and ξ

is a shape parameter [32]. The signal parameters (mean, width of Gaussian) and the shape parameter of the background function are free parameters of the fit. The data and the result of the fit are shown in Fig. 3(a). We fit the ΔE distribution of the selected $B^- \to D^+\pi^-\pi^-$ candidates with a sum of two Gaussian functions with a common mean for the signal and a linear function for the background. The signal parameters (mean, width of wide Gaussian, width and fraction of narrow Gaussian) and the slope of the background function are free parameters of the fit. The data and the result of the fit are shown in Fig. 3(b). The resulting signal yield is 3496 ± 74 events, where the error is statistical only. A clear signal is evident in both m_{ES} and ΔE distributions.

To distinguish signal and background in the Dalitz plot studies, we divide the candidates into three subsamples: the signal region, $-21 < \Delta E < 15$ MeV, the left sideband, $-109 < \Delta E < -73$ MeV, and the right sideband, $67 < \Delta E < 103$ MeV. The events in the signal region are used in the Dalitz plot analysis, while the events in the sideband regions are used to study the background.

In order to check the shape of the background ΔE distribution, we have generated a background MC sample of resonant and continuum events with $B^- \to D^+\pi^-\pi^-$ signal events removed. The background MC sample has been scaled to the same luminosity as the data. The ΔE distribution of the selected events from the background MC sample is shown as the histogram in Fig. 3(b). A small amount of peaking background is found from misreconstructed decays of $\bar{B}^0 \to D^+\rho^-$ with $\rho^- \to \pi^-\pi^0$, where a π^0 is missed and a random track in the event is misidentified as a signal π^-. The background histogram in Fig. 3(b) is fitted with a sum of two Gaussian functions with a common mean for the peaking background, with parameters fixed to those obtained from the fit to data, and a linear function to describe the combinatorial background. The amount of peaking background is estimated at 82 ± 41 events. After peaking background subtraction, the number of signal events above background is $N_{\text{signal}} = 3414 \pm 85$. The background fraction in the signal region is $(30.4 \pm 1.1)\%$.

IV. DALITZ PLOT ANALYSIS

We refit the D^+ and B^- candidate momenta by constraining the trajectories of the three daughters of the B^- meson candidate to originate from a common decay vertex while constraining the invariant masses of $K^-\pi^+\pi^+$ and $D^+\pi^-\pi^-$ to the D^+ and B^- masses [5], respectively. The mass-constraints ensure that all events fall within the Dalitz plot boundary.

In the decay of a B^- into a final state composed of three pseudoscalar particles ($D^+\pi^-\pi^-$), 2 degrees of freedom are required to describe the decay kinematics. In this analysis we choose the two $D\pi$ invariant mass-squared combinations $x = m^2(D^+\pi_1^-)$ and $y = m^2(D^+\pi_2^-)$ as the

FIG. 3 (color online). (a) m_{ES} and (b) ΔE distributions for $D^+\pi^-\pi^-$ candidates. Data (points with statistical errors) are compared to the results of the fits (solid curves), with the background contributions marked as dashed lines. The histograms are the corresponding distributions of the background MC sample as described in the text. The shaded area in (a) shows the signal region, while the three shaded areas in (b) mark the signal region in the center and the two sidebands.

independent variables, where the two like-sign pions π_1^- and π_2^- are randomly assigned to x and y. This has no effect on our analysis since the likelihood function (described below) is explicitly symmetrized with respect to interchange of the two identical particles.

The differential decay rate is generally given in terms of the Lorentz-invariant matrix element $\mathcal{M}$ by

$$\frac{d^2\Gamma}{dxdy} = \frac{|\mathcal{M}|^2}{256\pi^3 m_B^3}, \qquad (3)$$

where m_B is the B meson mass. The Dalitz plot gives a graphical representation of the variation of the square of the matrix element, $|\mathcal{M}|^2$, over the kinematically accessible phase space (x, y) of the process. Nonuniformity in the Dalitz plot can indicate presence of intermediate resonances, and their masses and spin quantum numbers can be determined.

A. Probability density function

We describe the distribution of candidate events in the Dalitz plot in terms of a probability density function (PDF). The PDF is the sum of signal and background components and has the form

$$\text{PDF}(x, y) = f_{\text{bg}} \frac{B(x, y)}{\int_{\text{DP}} B(x, y)dxdy} + (1 - f_{\text{bg}})$$
$$\times \frac{[S(x, y) \otimes \mathcal{R}]\epsilon(x, y)}{\int_{\text{DP}}[S(x, y) \otimes \mathcal{R}]\epsilon(x, y)dxdy}, \qquad (4)$$

where the integral is performed over the whole Dalitz plot, the $S(x, y) \otimes \mathcal{R}$ is the signal term convolved with the signal resolution function, $B(x, y)$ is the background term, f_{bg} is the fraction of background events, and ϵ is the reconstruction efficiency.

An unbinned maximum likelihood fit to the Dalitz plot is performed in order to maximize the value of

$$\mathcal{L} = \prod_{i=1}^{N_{\text{event}}} \text{PDF}(x_i, y_i) \qquad (5)$$

with respect to the parameters used to describe S, where x_i and y_i are the values of x and y for event i respectively, and N_{event} is the number of events in the Dalitz plot. In practice, the negative-log-likelihood (NLL) value

$$\text{NLL} = -\ln\mathcal{L} \qquad (6)$$

is minimized in the fit.

B. Goodness-of-fit

It is difficult to find a proper binning at the kinematic boundaries in the x-y plane of the Dalitz plot. For this reason, we choose to estimate the goodness-of-fit χ^2 in the $\cos\theta$ (range from -1 to 1) and $m_{\text{min}}^2(D\pi)$ (range from 4.04 to 15.23 GeV^2/c^4) plane, which is a rectangular representation of the Dalitz plot. The parameter θ is the helicity

angle of the $D\pi$ system and $m_{\text{min}}^2(D\pi)$ is the lesser of x and y. The helicity angle θ is defined as the angle between the momentum vector of the pion from the B decay (bachelor pion) and that of the pion of the $D\pi$ system in the $D\pi$ restframe.

The χ^2 value is calculated using the formula

$$\chi^2 = \sum_i \chi_i^2 = \sum_{i=1}^{n_{\text{total}}} \frac{(N_{\text{cell}i} - N_{\text{fit}i})^2}{N_{\text{fit}i}}, \qquad (7)$$

for cells in a 18×18 grid of the two-dimensional histogram. In Eq. (7), n_{total} is the total number of cells used, $N_{\text{cell}i}$ is the number of events in each cell, and $N_{\text{fit}i}$ is the expected number of events in that cell as predicted by the fit results. The number of degrees of freedom (NDF) is calculated as $n_{\text{total}} - k - 1$, where k is the number of free parameters in the fit. We require $N_{\text{fit}} \geq 10$; if this requirement is not met then neighboring cells are combined until ten events are accumulated.

C. Matrix element $\mathcal{M}$ and fit parameters

This analysis uses an isobar model formulation in which the signal decays are described by a coherent sum of a number of two-body ($D\pi$ system + bachelor pion) amplitudes. The orbital angular momentum between the $D\pi$ system and the bachelor pion is denoted here as L. The total decay matrix element $\mathcal{M}$ for $B^- \to D^+\pi^-\pi^-$ is given by

$$\mathcal{M} = \sum_{L=(0,1,2)} \rho_L e^{i\phi_L}[N_L(x, y) + N_L(y, x)]$$
$$+ \sum_k \rho_k e^{i\phi_k}[A_k(x, y) + A_k(y, x)], \qquad (8)$$

where the first term represents the S-wave ($L = 0$), P-wave ($L = 1$), and D-wave ($L = 2$) nonresonant contributions, the second term stands for the resonant contributions, the parameters ρ_k and ϕ_k are the magnitudes and phases of the kth resonance, while ρ_L and ϕ_L correspond to the magnitudes and phases of the nonresonant contributions with angular momentum L. The functions $N_L(x, y)$ and $A_k(x, y)$ are the amplitudes for nonresonant and resonant terms, respectively.

The resonant amplitudes $A_k(x, y)$ are expressed as

$$A_k(x, y) = R_k(m)F_L(p'r')F_L(qr)T_L(p, q, \cos\theta), \qquad (9)$$

where $R_k(m)$ is the kth resonance line shape, $F_L(p'r')$ and $F_L(qr)$ are the Blatt-Weisskopf barrier factors [33], and $T_L(p, q, \cos\theta)$ gives the angular distribution. The parameter $m(= \sqrt{x})$ is the invariant mass of the $D\pi$ system. The parameter p' is the magnitude of the three momentum of the bachelor pion evaluated in the B-meson rest frame. The parameters p and q are the magnitudes of the three momenta of the bachelor pion and the pion of the $D\pi$ system, both in the $D\pi$ rest frame. The parameters p', p, q, and θ are functions of x and y.

The nonresonant amplitudes $N_L(x, y)$ with $L = 0, 1, 2$ are similar to $A_k(x, y)$ but do not contain resonant mass terms:

$$N_0(x, y) = 1, \tag{10}$$

$$N_1(x, y) = F_1(p'r')F_1(qr)T_1(p, q, \cos\theta), \tag{11}$$

$$N_2(x, y) = F_2(p'r')F_2(qr)T_2(p, q, \cos\theta). \tag{12}$$

The Blatt-Weisskopf barrier factors $F_L(p'r')$ and $F_L(qr)$ depend on a single parameter, r' or r, the radius of the barrier, which we take to be 1.6 $(\text{GeV}/c)^{-1}$, similarly to Ref. [12]. A discussion of the systematic uncertainty associated with the choice of the values of r and r' follows below. The forms of $F_L(z)$, where $z = p'r'$ or qr, for $L = 0, 1, 2$ are

$$F_0(z) = 1, \tag{13}$$

$$F_1(z) = \sqrt{\frac{1 + z_0^2}{1 + z^2}}, \tag{14}$$

$$F_2(z) = \sqrt{\frac{9 + 3z_0^2 + z_0^4}{9 + 3z^2 + z^4}}, \tag{15}$$

where $z_0 = p'_0 r'$ or $q_0 r$. Here p'_0 and q_0 represent the values of p' and q, respectively, when the invariant mass is equal to the pole mass of the resonance. For nonresonant terms, the fit results are not affected by the choice of invariant mass (we use the sum of m_D and m_π) used for the calculations of p'_0 and q_0. For virtual D_v^* decay, $D_v^* \to D^+\pi^-$, and virtual B_v^* production in $B^- \to B_v^*\pi^-$, we use an exponential form factor in place of the Blatt-Weisskopf barrier factor, as discussed in Ref. [12]:

$$F(z) = \exp(-(z - z')), \tag{16}$$

where $z' = rp_v$ for $D_v^* \to D^+\pi^-$ and $z' = r'p_v$ for $B^- \to B_v^*\pi^-$. Here, we set $p_v = 0.038$ GeV$/c$, which gives the best fit, although any value of p_v between 0.015 and 1.5 GeV$/c$ gives a negligible effect on the fitted parameters compared to their statistical errors.

The resonance mass term $R_k(m)$ describes the intermediate resonance. All resonances in this analysis are parametrized with relativistic Breit-Wigner functions:

$$R_k(m) = \frac{1}{(m_0^2 - m^2) - im_0\Gamma(m)}, \tag{17}$$

where the decay width of the resonance depends on m:

$$\Gamma(m) = \Gamma_0\left(\frac{q}{q_0}\right)^{2L+1}\left(\frac{m_0}{m}\right)F_L^2(qr), \tag{18}$$

where m_0 and Γ_0 are the values of the resonance pole mass and decay width, respectively.

The terms $T_L(p, q, \cos\theta)$ describe the angular distribution of final-state particles and are based on the Zemach tensor formalism [34]. The definitions of $T_L(p, q, \cos\theta)$ for $L = 0, 1, 2$ are

$$T_0(p, q, \cos\theta) = 1, \tag{19}$$

$$T_1(p, q, \cos\theta) = -2pq\cos\theta, \tag{20}$$

$$T_2(p, q, \cos\theta) = 4p^2q^2(\cos^2\theta - 1/3). \tag{21}$$

The signal function is then given by

$$S(x, y) = |\mathcal{M}|^2. \tag{22}$$

In this analysis, the masses of D_v^* and B_v^* are taken from the world averages [5] while their widths are fixed at 0.1 MeV; the magnitude ρ_k and phase ϕ_k of the D_2^{*0} amplitude are fixed to 1 and 0, respectively, while the masses and widths of D_J^0 resonances and other magnitudes and phases are free parameters to be determined in the fit. The effect of varying the masses of D_v^* and B_v^* within their errors [5] and widths of D_v^* and B_v^* between 0.001 and 0.3 MeV is negligible compared to the other model-dependent systematic uncertainties given below.

Since the choice of normalization, phase convention, and amplitude formalism may not always be the same for different experiments, we use fit fractions and relative phases instead of amplitudes to allow for a more meaningful comparison of results. The fit fraction for the kth decay mode is defined as the integral of the resonance decay amplitudes divided by the coherent matrix element squared for the complete Dalitz plot:

$$f_k = \frac{\int_{\text{DP}} |\rho_k(A_k(x, y) + A_k(y, x))|^2 dxdy}{\int_{\text{DP}} |\mathcal{M}|^2 dxdy}. \tag{23}$$

The fit fraction for nonresonant term with angular momentum L has a similar form:

$$f_L = \frac{\int_{\text{DP}} |\rho_L(N_L(x, y) + N_L(y, x))|^2 dxdy}{\int_{\text{DP}} |\mathcal{M}|^2 dxdy}. \tag{24}$$

The fit fractions do not necessarily add up to unity because of interference among the amplitudes.

To estimate the statistical uncertainties on the fit fractions, the fit results are randomly modified according to the covariance matrix of the fit and the new fractions are computed using Eq. (23) or (24). The resulting fit fraction distribution is fitted with a Gaussian whose width gives the error on the given fraction.

D. Signal resolution function

The detector has finite resolution, thus measured quantities differ from their true values. For the narrow resonance D_2^* with the expected width of about 40 MeV, the signal resolution needs to be taken into account. In order to obtain the signal resolution on $m^2(D\pi)$ around the D_2^* mass region, we study a sample of MC generated $B^- \to X\pi^- \to D^+\pi^-\pi^-$ decays, with the mass and width of X set to 2.460 GeV$/c^2$ (D_2^* mass region) and 0 MeV, respectively,

and subject these events to the same analysis reconstruction chain. The reconstructed events are then classified into two categories: truth-matched (TM) events, where the B and the daughters are correctly reconstructed, and self-crossfeed (SCF) events, where one or more of the daughters is not correctly associated with the generated particle.

The two-dimensional distribution of $\cos\theta$ versus $m^2(D\pi)$ for truth-matched events is shown in Fig. 4. Since the resolution is independent of $\cos\theta$, we fit the distribution of the quantity $q' = m^2(D\pi) - m^2_{\text{true}}$ using a sum of two Gaussian functions with a common mean to obtain the resolution function for truth-matched events ($\mathcal{R}_{\text{TM}}$). The signal resolution for an invariant mass of the $D\pi$ combination around the D_2^{*0} region is about 3 MeV/c^2.

The two-dimensional distribution of $\cos\theta$ versus $m^2(D\pi)$ for self-crossfeed events is shown in Fig. 5. The SCF fraction, f_{SCF}, varies from 0.5% to 4.0% with $\cos\theta$. We fit the f_{SCF} distribution with a fourth-order polynomial function. The f_{SCF} distribution and the result of the fit are shown in Fig. 6. The resolution for self-crossfeed events varies between 5 MeV/c^2 and 100 MeV/c^2 with $\cos\theta$. We divide the $\cos\theta$ interval into 40 bins of equal width and use these bins to describe the resolution function ($\mathcal{R}_{\text{SCF}}$) in terms of a sum of two bifurcated Gaussian (BGaussian) functions with different means. The BGaussian is a Gaussian as a function of q' with three parameters, q_0' the mean, and the two widths, σ_1 on the left and σ_2 on the right side of the mean. The form of BGaussian is

$$\text{BGaussian}(q' - q_0', \sigma_1, \sigma_2)$$

$$= \begin{cases} \frac{2}{\sqrt{2\pi}(\sigma_1 + \sigma_2)} \exp\left(-\frac{(q' - q_0')^2}{2\sigma_1^2}\right) & \text{if } q' < q_0'; \\ \frac{2}{\sqrt{2\pi}(\sigma_1 + \sigma_2)} \exp\left(-\frac{(q' - q_0')^2}{2\sigma_2^2}\right) & \text{if } q' \geq q_0', \end{cases} \quad (25)$$

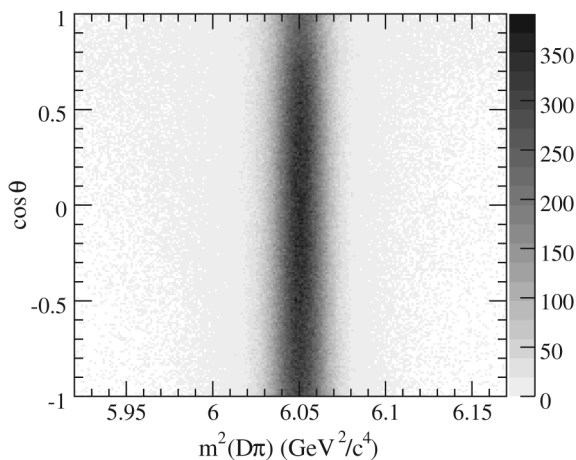where q_0', σ_1, and σ_2 are free parameters.

FIG. 4. Two-dimensional histogram $\cos\theta$ versus $m^2(D\pi)$ of the truth-matched events as defined in the text.
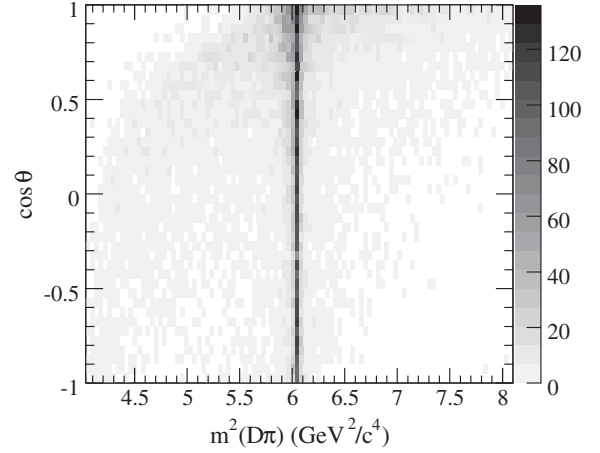

FIG. 5. Two-dimensional histogram $\cos\theta$ versus $m^2(D\pi)$ of the self-crossfeed events as defined in the text.

The signal resolution function is then given by

$$\mathcal{R}(q', \cos\theta) = (1 - f_{\text{SCF}}(\cos\theta)) \times \mathcal{R}_{\text{TM}}(q')$$
$$+ f_{\text{SCF}}(\cos\theta) \times \mathcal{R}_{\text{SCF}}(q', \cos\theta). \quad (26)$$

The function $\mathcal{R}(q', \cos\theta)$ represents the probability density for an event having the true mass-squared m^2_{true} to be reconstructed at $m^2(D\pi)$ for different $\cos\theta$ regions.

The signal term S in Eq. (4) is convoluted with the above resolution function. For each event, the convolution is performed using numerical integration:

$$S(x, y) \otimes \mathcal{R} = \int S(q_{\min} + q', q'_{\max}) \times \mathcal{R}(q', \cos\theta)dq', \quad (27)$$

where S is the signal function in Eq. (22) and $q_{\min}$ ($q_{\max}$) is the lesser (greater) of x and y. The quantity $\cos\theta$ is determined from $q_{\min}$ and $q_{\max}$ and is assumed to be constant during convolution. The resolution in $\cos\theta$ has a negligible effect on the fitted parameters. The quantity $q'_{\max}$ is computed using the kinematics of three-body decay with $q_{\min}$, q', and $\cos\theta$.
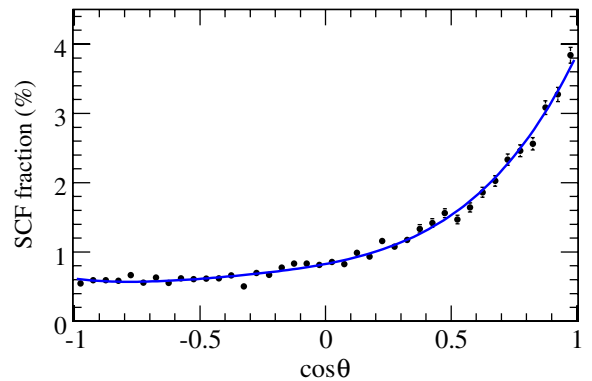

FIG. 6 (color online). $f_{\text{SCF}}(\cos\theta)$ distribution. The observed self-crossfeed fractions (points with statistical errors) are compared to the results of the fit (solid curve).

The resolution function and the integration method in Eq. (27) have been fully tested using 262 MC samples with full event reconstruction given below. We have compared D invariant mass resolutions for $D^0 \to K^- \pi^+$, $K^- \pi^+ \pi^- \pi^+$, and $D^+ \to K^- \pi^+ \pi^+$ between data and MC-simulated events and find that they agree within their statistical uncertainties. Estimated biases in the fitted parameters due to uncertainties in the signal resolution function are small and have been included into the systematic errors.

E. Efficiency

The signal term S defined above is modified in order to take into account experimental particle detection and event reconstruction efficiency. Since different regions of the Dalitz plot correspond to different event topologies, the efficiency is not expected to be uniform over the Dalitz plot. The term $\epsilon(x, y)$ in Eq. (4) is the overall efficiency for truth-matched and self-crossfeed signal events, hence the efficiency for truth-matched signal events is

$$\epsilon_{\text{TM}}(x, y) = \epsilon(x, y)(1 - f_{\text{SCF}}(\cos\theta)). \qquad (28)$$

In order to determine the efficiency across the Dalitz plot, a sample of simulated $B^- \to D^+ \pi^- \pi^-$ events in the Dalitz plot is generated. Some events are generated with one or more additional final-state photons to account for radiative corrections [35]. As a result, the generated Dalitz plot is slightly distorted from the uniform distribution. The number of generated events is $N_{\text{gen}} = 1252k$. Each event is subjected to the standard reconstruction and selection, described in Sec. III. In addition, we require that the candidate decay is truth matched. After correcting for data/MC efficiency differences in particle identification, which are momentum dependent and thus vary over the Dalitz plot, the total number of accepted events is $N_{\text{acc}} = 121\,390$. We employ an unbinned likelihood method to fit the Dalitz plot distributions for generated and accepted event samples. The PDF for generated events (PDF_{gen}) is a fourth-order two-dimensional polynomial while the PDF for accepted events (PDF_{acc}) is a seventh-order two-dimensional polynomial. The efficiency function is then given by

$$\epsilon_{\text{TM}}(x, y) = \frac{\text{PDF}_{\text{acc}}(x, y) \times N_{\text{acc}}}{\text{PDF}_{\text{gen}}(x, y) \times N_{\text{gen}}}. \qquad (29)$$

Figure 7 shows the efficiency as a function of $m^2(D\pi)$ and the fit result for MC-simulated events.

F. Background

The background distribution is modeled using MC background events, selected with the same criteria applied to the data and requiring the B candidate to fall into the signal ΔE region defined in Sec. III. Events in the data ΔE sidebands could also be used to model the background,
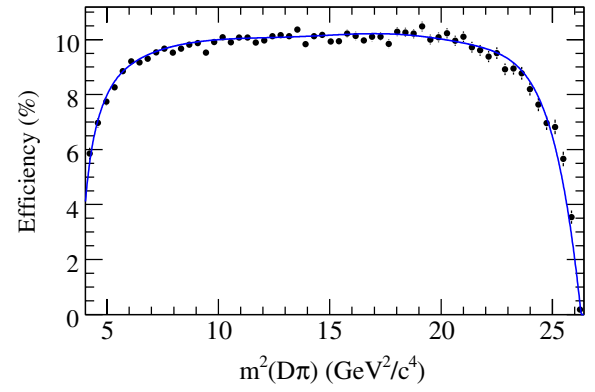
FIG. 7 (color online). The efficiency for signal decays as a function of $m^2(D\pi)$, as determined by MC simulation (points with statistical errors) and the results of the fit to the accepted and generated distributions (solid curve).
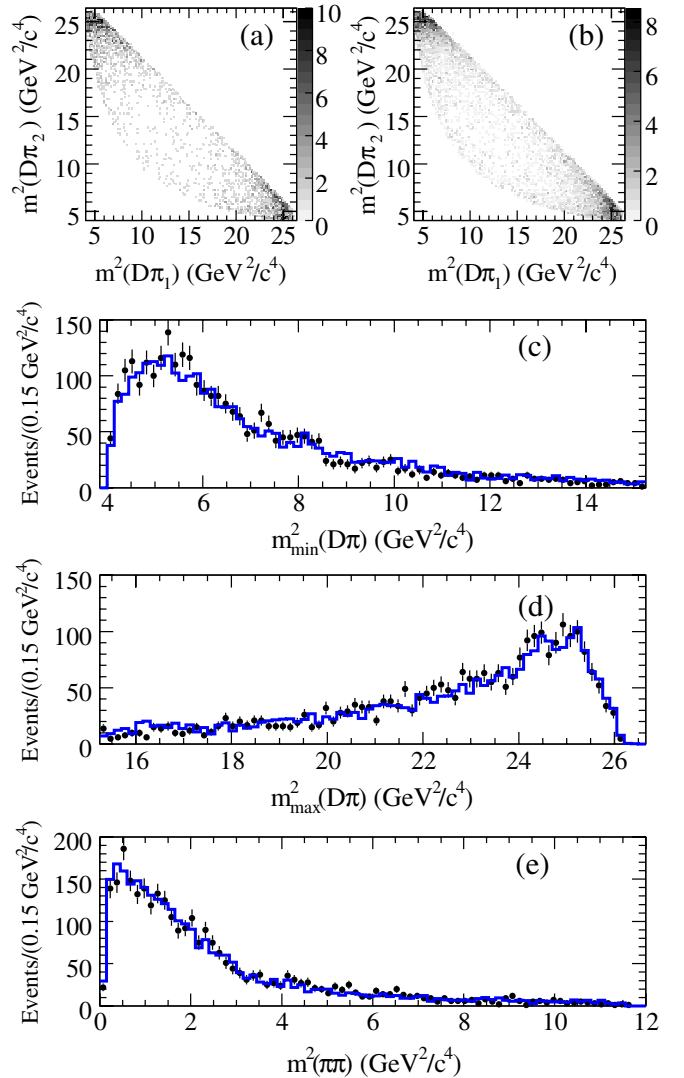
FIG. 8 (color online). Comparison of events in the ΔE sideband: Dalitz plot for (a) data and (b) MC-simulated events, and projections on (c) $m^2_{\text{min}}(D\pi)$, (d) $m^2_{\text{max}}(D\pi)$, and (e) $m^2(\pi\pi)$ with data (points with statistical errors) and MC predictions (histograms).

FIG. 9 (color online). Fit to background events in the ΔE signal region of the MC sample: (a) Dalitz plot and projections on (b) $m_{min}^2(D\pi)$, (c) $m_{max}^2(D\pi)$, and (d) $m^2(\pi\pi)$ with MC predictions (points with statistical errors) and the fits (solid curves).

however in MC studies we find differences between the Dalitz plot distributions of the background in the signal and sideband regions. Since we find the Dalitz plot distributions of sideband events in data and in the MC simulation to be 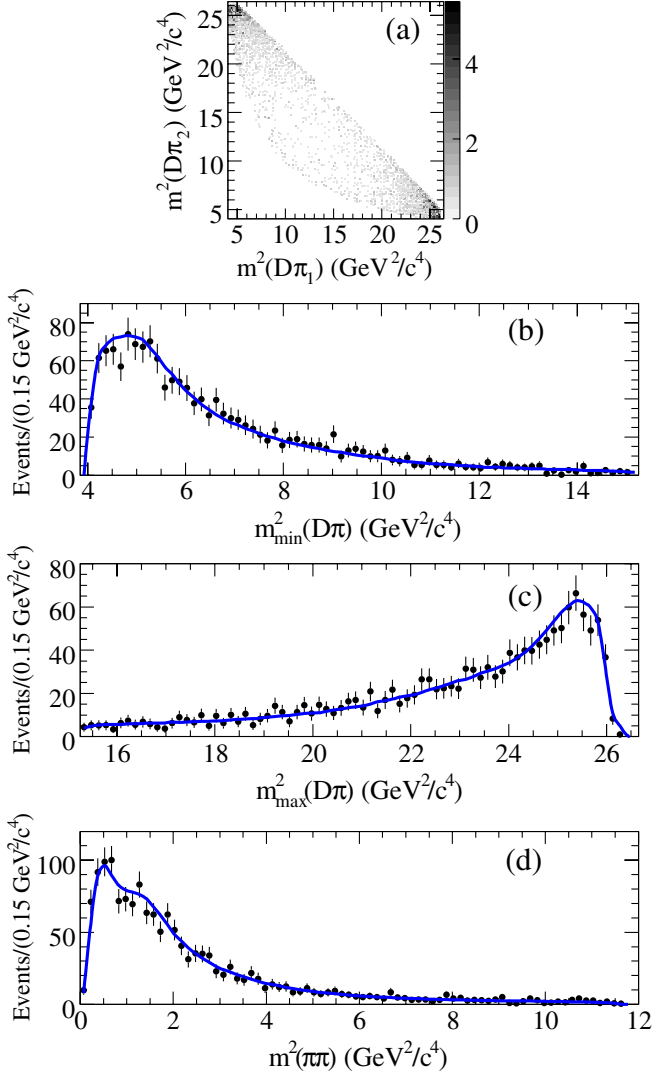consistent within their statistics, we are confident that the MC simulation can accurately represent the background distribution in the signal region. Figures 8(a), 8(b), and 9(a) show the Dalitz plot distributions of sideband events in data, sideband events in the MC sample and background events in the ΔE signal region of the MC sample, respectively. Figures 8(c)–8(e) show the comparisons of ΔE sideband events between data and MC simulation in $m_{min}^2(D\pi)$, $m_{max}^2(D\pi)$, and $m^2(\pi\pi)$ projections, respectively. Here $m_{min}^2(D\pi)$ ($m_{max}^2(D\pi)$) is the lesser (greater) of x and y.

The parametrization used to describe the background is

$$
\begin{aligned}
B(x, y) = {} & c_0(q_{min} - q_1)^{c_1} \times \exp(c_2(q_{min} - q_1) \\
& + c_3(q_{min} - q_1)^2) + c_4(q_2 - q_{max})^{c_5} \\
& \times \exp(c_6(q_2 - q_{max}) + c_7(q_2 - q_{max})^2) \\
& + c_8(z - z_1))^{c_9} \exp(c_{10}(z - z_1) + c_{11}(z - z_1)^2) \\
& + c_{15}\text{BGaussian}(q_{max} - c_{12}, c_{13}, c_{14}) \\
& + c_{19}\text{BGaussian}(z - c_{16}, c_{17}, c_{18}),
\end{aligned}
\tag{30}
$$

where the coefficients c_0 to c_{19} are free parameters to be determined from the fit, $q_1 = (m_D + m_\pi)^2 = 4.04 \text{ GeV}^2/c^4$ and $q_2 = (m_B - m_\pi)^2 = 26.41 \text{ GeV}^2/c^4$ are the lower and upper limits of the Dalitz plot, respectively, $z_1 = (2m_\pi)^2 = 0.077 \text{ GeV}^2/c^4$ is the lower limit of $m^2(\pi\pi)$, q_{min} is the lesser of x and y, q_{max} is the greater of x and y, z is the invariant $m^2(\pi\pi)$, and BGaussian is given in Eq. (25).

The projections on $m_{min}^2(D\pi)$, $m_{max}^2(D\pi)$, and $m^2(\pi\pi)$ and the result of the fit for the background events in the signal region of the MC sample are shown in Figs. 9(b)–9(d). The χ^2/NDF for the fit is $72/64$.

V. RESULTS

A. Branching fraction $\mathcal{B}(B^- \to D^+ \pi^- \pi^-)$

The total $B^- \to D^+ \pi^- \pi^-$ branching fraction is calculated using the relation:

$$
\mathcal{B} = \frac{N_{signal}}{(\bar{\epsilon} \cdot \mathcal{B}(D^+)) \cdot 2N(B^+ B^-)},
\tag{31}
$$

where $N_{signal} = 3414 \pm 85$ is the fitted signal yield given in Sec. III, $\bar{\epsilon}$ is the average efficiency, $\mathcal{B}(D^+) = (9.22 \pm 0.21)\%$ is the branching fraction for $D^+ \to K^- \pi^+ \pi^+$ [5,36], and the total number of $B^+ B^-$ events, $N(B^+ B^-) = (197.2 \pm 3.1) \times 10^6$, is determined using $N_{B\bar{B}}$ and the ratio of $\Gamma(\Upsilon(4S) \to B^+ B^-)/\Gamma(\Upsilon(4S) \to B^0 \bar{B})$ ($= 1.065 \pm 0.026$) [5].

Since the reconstruction efficiencies vary slightly for different resonances, the average efficiency is calculated by weighing the accepted and generated events by $S(x, y)$ with the values for the parameters of our nominal Dalitz plot model (discussed below):

$$
\bar{\epsilon} = \frac{\sum_{i=1}^{N_{acc}} S(x_i, y_i) \times w_i}{\sum_{j=1}^{N_{gen}} S(x_j, y_j)},
\tag{32}
$$

where w_i is the correction factor which depends on x and y due to particle identification efficiency. The value $\bar{\epsilon} = (8.72 \pm 0.05)\%$ is obtained using this method.

The measured total branching fraction is $\mathcal{B}(B^- \to D^+ \pi^- \pi^-) = (1.08 \pm 0.03) \times 10^{-3}$, where the stated error refers to the statistical uncertainty only. A full discussion of the systematic uncertainties follows below.
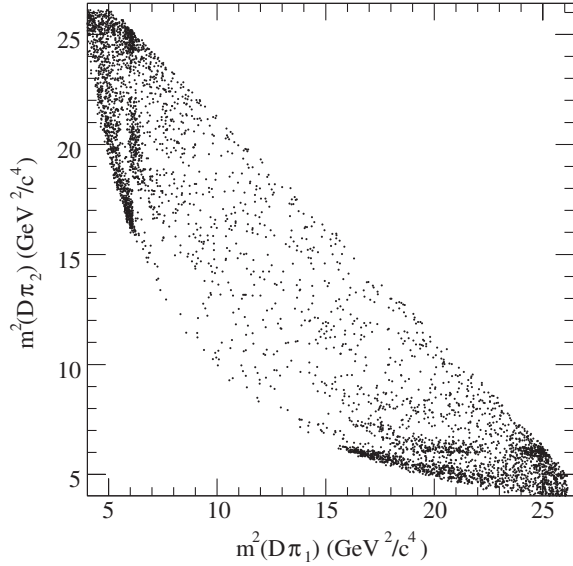
FIG. 10. Data Dalitz plot for $B^- \to D^+ \pi^- \pi^-$.

B. Dalitz plot analysis results

The Dalitz plot distribution for data is shown in Fig. 10. Since the composition of events in the Dalitz plot and their distributions are not known *a priori*, we have tried a variety of different assumptions. In particular, we test the inclusion of various components, such as the virtual D_v^* and B_v^* as well as S-, P-, and D-wave modeling of the nonresonant component, in addition to the expected components of D_2^{*0},

D_0^{*0}, and background. The D-wave nonresonant term does not improve the goodness-of-fit and the fraction of D-wave nonresonant contribution is close to 0. The results of these tests with variations of the models are summarized in Table II. Of these models, model 1 produces the best fit quality with the smallest number of components, and we choose it as the nominal fit model. The components considered in this fit model are D_2^{*0}, D_0^{*0}, D_v^*, B_v^*, and P-wave nonresonant. The P-wave nonresonant component is an addition to the fit model used in the previous measurement from Belle [12]. The sum of the fractions $(115 \pm 5)\%$ for the nominal fit differs from 100% because of destructive interferences among the amplitudes. The χ^2/NDF for the nominal fit is $220/153$. To better understand the large χ^2/NDF, we look at the contributions to the total χ^2 from individual cells. We find four cells with $\chi^2 > 7$, which inflate the total χ^2. The central points in these cells are at $(6.83, -0.722)$, $(6.83, -0.611)$, $(6.83, 0.5)$, and $(8.08, -0.722)$, where the first value is $m^2_{\min}(D\pi)$ and the second is $\cos\theta$. In order to determine the effect on the fitted parameters from these cells, we repeat the nominal fit with these cells excluded. The resulting χ^2/NDF is $182/149$, corresponding to a probability of 3.4%. Assuming these large χ^2 contributions are caused by an unknown systematic problem, removing them from the fit is reasonable. However, under the assumption that these high χ^2 contributions have a statistical origin, the χ^2 probability is 0.04% [37]. The low probability indicates that a model more complex than the isobar model may be necessary to describe the characteristics of the data. The differences in the

TABLE II. Fit results for the masses, widths, fit fractions, and phases from the Dalitz plot analysis of $B^- \to D^+ \pi^- \pi^-$ for different models. The errors are statistical only. The magnitude and phase of the D_2^{*0} amplitude are fixed to 1 and 0, respectively. The background fraction is fixed to 30.4% as described in Sec. III. The nominal fit corresponds to model 1. The labels, S-NR and P-NR, denote the S-wave nonresonant and P-wave nonresonant contributions, respectively.

Parameter	Model 1	Model 2	Model 3	Model 4	Model 5	Model 6	Model 7
$m_{D_2^{*0}}$ (MeV/c^2)	2460.4 ± 1.2	2460.2 ± 1.0	2459.1 ± 1.0	2460.1 ± 1.1	2461.5 ± 1.2	2458.1 ± 1.1	2457.4 ± 1.0
$\Gamma_{D_2^{*0}}$ (MeV)	41.8 ± 2.5	41.7 ± 2.4	41.1 ± 2.4	41.8 ± 2.4	42.0 ± 2.5	41.8 ± 2.4	41.7 ± 2.4
$m_{D_0^{*0}}$ (MeV/c^2)	2297 ± 8	2309 ± 7	2297 ± 7	2312 ± 10	2307 ± 11	2270 ± 8	2273 ± 5
$\Gamma_{D_0^{*0}}$ (MeV)	273 ± 12	285 ± 11	288 ± 12	289 ± 20	313 ± 21	262 ± 12	276 ± 10
$f_{D_2^{*0}}$ (%)	32.2 ± 1.3	30.8 ± 1.2	31.5 ± 1.1	30.7 ± 1.5	32.6 ± 1.3	32.9 ± 1.3	30.9 ± 1.1
$\phi_{D_2^{*0}}$ (rad)	0.0 (fixed)	0.0 (fixed)	0.0 (fixed)	0.0 (fixed)	0.0 (fixed)	0.0 (fixed)	0.0 (fixed)
$f_{D_0^{*0}}$ (%)	62.8 ± 2.5	59.0 ± 2.1	57.5 ± 1.7	57.0 ± 4.5	88.0 ± 8.1	64.8 ± 2.2	69.7 ± 1.1
$\phi_{D_0^{*0}}$ (rad)	-2.07 ± 0.06	-2.06 ± 0.05	-2.01 ± 0.05	-2.00 ± 0.12	-2.14 ± 0.10	-1.96 ± 0.06	-2.00 ± 0.05
$f_{D_v^*}$ (%)	10.1 ± 1.4	11.3 ± 1.5	9.0 ± 1.2	11.0 ± 1.5	9.6 ± 1.3		
$\phi_{D_v^*}$ (rad)	3.00 ± 0.12	2.99 ± 0.08	3.17 ± 0.10	3.05 ± 0.12	2.82 ± 0.17		
$f_{B_v^*}$ (%)	4.6 ± 2.6	1.4 ± 0.5		1.7 ± 0.8	12.2 ± 5.4	2.2 ± 1.4	
$\phi_{B_v^*}$ (rad)	2.80 ± 0.21	-2.43 ± 0.28		-2.33 ± 0.28	2.52 ± 0.25	2.28 ± 0.38	
$f_{\mathrm{P-NR}}$ (%)	5.4 ± 2.4		1.6 ± 0.4		12.6 ± 4.0	12.7 ± 3.1	
$\phi_{\mathrm{P-NR}}$ (rad)	-0.89 ± 0.18		-1.46 ± 0.20		-0.84 ± 0.12	-0.71 ± 0.10	
$f_{\mathrm{S-NR}}$ (%)				0.3 ± 0.3	5.2 ± 3.8		
$\phi_{\mathrm{S-NR}}$ (rad)				-0.77 ± 0.49	3.30 ± 0.23		
f_{bg} (%)	30.4 (fixed)	30.4 (fixed)	30.4 (fixed)	30.4 (fixed)	30.4 (fixed)	30.4 (fixed)	30.4 (fixed)
NLL	22970	22982	22977	22982	22964	23046	23125
χ^2/NDF	220/153	240/152	236/154	239/153	216/150	328/160	454/161

fitted D_2^* and D_0^* parameters, when these cells are included or excluded, are assigned to systematic uncertainties and are much smaller than the statistical uncertainties. The removal of these cells does not affect the choice of model 1 as the nominal fit from Table II.

Reference [38] argues for an addition of a $D\pi$ S-wave state near the $D\pi$ system threshold to the model of the $D\pi\pi$ final state. We have performed tests using the models 1–4 in Table II with the D_v^* replaced by a $D\pi$ S-wave state. Two different parametrizations for $D\pi$ S-wave state am-

plitude are used: one is the function given by Eq. (8) of Ref. [38] with the numerator set to constant, the other function is the relativistic Breit-Wigner given by Eq. (17). Among the tests we have performed with these parametrizations, the model with D_2^*, D_0^*, $D\pi$ S-wave (using Eq. (8) of Ref. [38]), B_v^* and P-wave nonresonant gives the best fit with NLL and χ^2/NDF values of 22 997 and 271/151, respectively, which are worse than those of the nominal fit even when allowing the $D\pi$ S-wave's parameters to vary. Each of these models also requires large fractions of D_0^*.

The nominal fit model results in the following branching fractions: $\mathcal{B}(B^- \rightarrow D_2^{*0}\pi^-) \times \mathcal{B}(D_2^{*0} \rightarrow D^+\pi^-) = (3.5 \pm 0.2) \times 10^{-4}$ and $\mathcal{B}(B^- \rightarrow D_0^{*0}\pi^-) \times \mathcal{B}(D_0^{*0} \rightarrow D^+\pi^-) = (6.8 \pm 0.3) \times 10^{-4}$, where the errors are statistical only. A full discussion of the systematic uncertainties follows below.

Figures 11(a)–11(c) show the $m_{min}^2(D\pi)$, $m_{max}^2(D\pi)$, and $m^2(\pi\pi)$ projections, respectively, while Figs. 12(a) and 12(b) show the $\cos\theta$ distributions for the D_0^{*0} and D_2^{*0} mass regions, respectively. The distributions in Figs. 11 and 12 show good agreement between the data and the fit. The angular distribution in the D_2^{*0} mass region
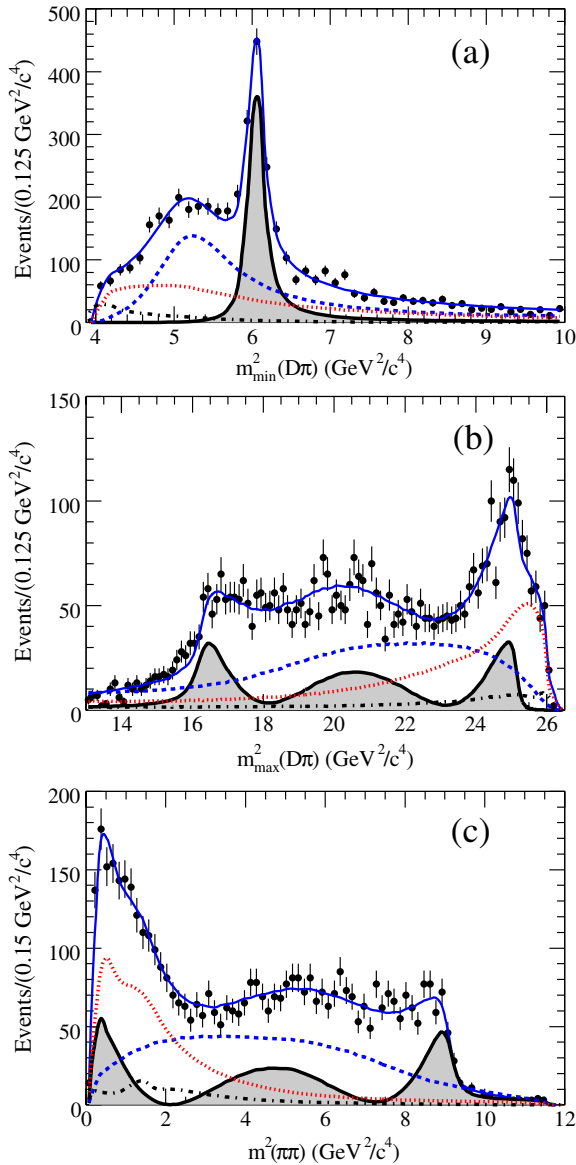

FIG. 11 (color online). Result of the nominal fit to the data: projections on (a) $m_{min}^2(D\pi)$, (b) $m_{max}^2(D\pi)$, and (c) $m^2(\pi\pi)$. The points with error bars are data, the solid curves represent the nominal fit. The shaded areas show the D_2^{*0} contribution, the dashed curves show the D_0^{*0} signal, the dash-dotted curves show the D_v^* and B_v^* signals, and the dotted curves show the background.
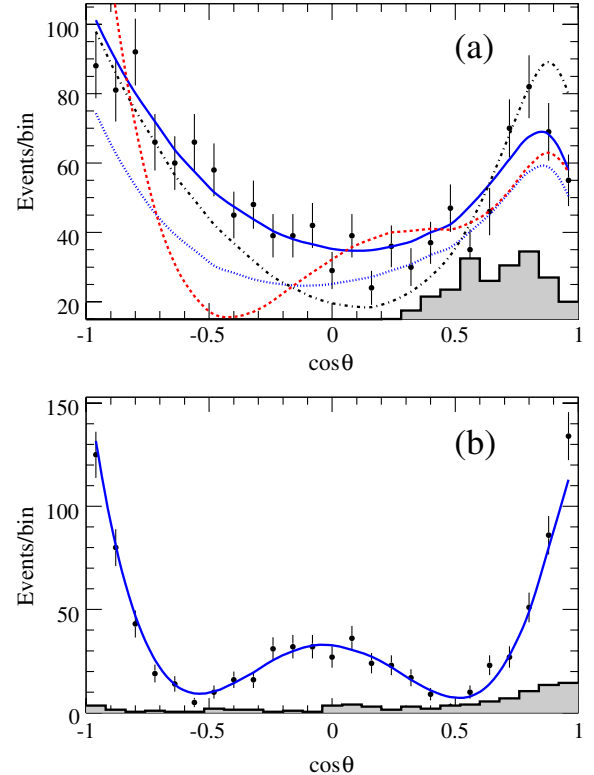

FIG. 12 (color online). Result of the nominal fit to the data: the $\cos\theta$ distributions for (a) $4.5 < m^2(D\pi) < 5.5$ GeV$^2/c^4$ region and (b) $5.9 < m^2(D\pi) < 6.2$ GeV$^2/c^4$ region. The points with error bars are data, the solid curves represent the nominal fit. The dashed, dash-dotted, and dotted curves in (a) show the fit of hypotheses 2–4 in Table III, respectively. The shaded histograms show the $\cos\theta$ distributions from ΔE sidebands in data.

TABLE III. Comparison of the models with different resonances composition. The labels, S-NR and P-NR, denote the S-wave nonresonant and P-wave nonresonant contributions, respectively.

Hypothesis	Model	NLL	χ^2/NDF
	Model 1 (nominal fit)	22 970	220/153
1	D_2^{*0}, D_v^*, B_v^*, P-NR	23 761	1171/143
2	D_2^{*0}, D_v^*, B_v^*, P-NR, (2^+)	23 699	991/144
3	D_2^{*0}, D_v^*, B_v^*, P-NR, (1^-)	23 427	638/135
4	D_2^{*0}, D_v^*, B_v^*, P-NR, S-NR	23 339	652/157

is clearly visible and is consistent with the expected D-wave distribution of $|\cos^2\theta - 1/3|^2$ for a spin-2 state. In addition, the D_0^{*0} signal and the reflection of D_2^{*0} can be easily distinguished in the $m_{\min}^2(D\pi)$ and $m_{\max}^2(D\pi)$ projection, respectively. The lower edge of $m_{\min}^2(D\pi)$ is better described with D_v^* component included than without.

Table III shows the NLL and χ^2/NDF values for the nominal fit and for the fits with the broad resonance D_0^{*0} excluded or with the J^P of the broad resonance replaced by other quantum numbers. In all cases, the NLL and χ^2/NDF values are significantly worse than that of the nominal fit. Figure 12(a) illustrates the helicity distributions in the D_0^{*0} mass region from hypotheses 2–4; clearly the nominal fit gives the best description of the data. We conclude that a broad spin-0 state D_0^{*0} is required in the fit to the data. The same conclusion is obtained when performing the same test on Models 2–5.

VI. SYSTEMATIC UNCERTAINTIES

A. Uncertainties on $\mathcal{B}(B^- \to D^+ \pi^- \pi^-)$

As listed in Table IV, the systematic error on the measurement of the total $B^- \to D^+ \pi^- \pi^-$ branching fraction is due to the uncertainties on the following quantities: the number of B^+B^- events in the initial sample, the charged track reconstruction and identification efficiencies, and the $D^+ \to K^- \pi^+ \pi^+$ branching fraction. The uncertainty in the ΔE background shape, the uncertainty in the average

TABLE IV. Summary of systematic uncertainties (relative errors in %) in the measurement of the total branching fraction.

Systematic source	$\frac{\Delta \mathcal{B}(B^- \to D^+ \pi^- \pi^-)}{\mathcal{B}(B^- \to D^+ \pi^- \pi^-)}$ (%)
Number of B^+B^- events	1.6
Tracking efficiencies	2.5
PID	1.5
ΔE background shape	1.3
D^+ branching fraction	2.3
Fit models	0.7
Fit bias	1.0
Total systematics	4.4

efficiency due to the fit models, and a possible fit bias also contribute to the systematic error.

The uncertainty on the number of B^+B^- events is determined using the uncertainties on $\Gamma(\Upsilon(4S) \to B^+B^-)/\Gamma(\Upsilon(4S) \to B^0\bar{B}^0)$ [5] and integrated luminosity (1.1%). The uncertainty on the input D^+ branching fraction is taken from [36]. The uncertainty in the ΔE background shape is estimated by comparing the signal yields between fitting the ΔE distribution with a linear background shape and with higher-order (second and third-order) polynomials. The uncertainty in the fit models is estimated by comparing the average efficiencies in Eq. (32) using Models 2–5 of Table II. The fit bias is estimated to be less than 1% by comparing the generated and the fitted value of $\mathcal{B}(B^- \to D^+ \pi^- \pi^-)$ from resonant and continuum MC samples.

B. Uncertainties on Dalitz plot analysis results

The sources of systematic uncertainties that affect the results of the Dalitz plot analysis are summarized in Table V. These uncertainties are added in quadrature, as they are uncorrelated, to obtain the total systematic error.

The uncertainties due to the background parametrization are estimated by comparing the results from the nominal fit with those obtained when the background shape parameters are allowed to float in the fit. The errors from the uncertainty in the background fraction are estimated by comparing the fit results when the background fraction is changed by its statistical error. We vary the set of cuts on ΔE, m_{ES}, R_2, $\cos\Theta_{\mathrm{th}}$, and mass of D^+, which increase the number of signal events by 25% and the background fraction to 36.5%, and repeat the fits. The difference in the fit results is taken as an estimate of the systematic uncertainty due to the event selection. Fit biases are studied using 1248 parametrized MC samples and 262 MC samples with full event reconstruction. Small biases are observed for some of the parameters. We combine these biases with those coming from high χ^2 cells, as discussed in the previous section, in quadrature to obtain the total systematic contribution from the fit bias. The uncertainties in PID are obtained by comparing the nominal fit results with those obtained when the PID corrections to the reconstruction efficiency are varied according to their uncertainties. The uncertainties in the efficiency and signal resolution parametrization are found to be negligible using the fits to the reconstructed MC samples.

In addition to the above systematic uncertainties, we also estimate a model-dependent uncertainty that comes from the uncertainty in the composition of the signal model and the uncertainty in the Blatt-Weisskopf barrier factors. The model-dependent uncertainties are estimated by comparing the fit results with Models 2–5 in Table II and by varying the radius of the barrier, r' and r in Eqs. (14)–(16) from 0 to 5 $(\mathrm{GeV}/c)^{-1}$.

TABLE V. Summary of systematic uncertainties in the masses, widths, and fit fractions of the D_2^{*0} and D_0^{*0} and the phase of D_0^{*0}.

Systematic source	$\Delta m_{D_2^{*0}}$ (MeV/c^2)	$\Delta \Gamma_{D_2^{*0}}$ (MeV)	$\Delta m_{D_0^{*0}}$ (MeV/c^2)	$\Delta \Gamma_{D_0^{*0}}$ (MeV)	$\Delta f_{D_2^{*0}}$ (%)	$\Delta f_{D_0^{*0}}$ (%)	$\Delta \phi_{D_0^{*0}}$ (rad)
Background parametrization	1.0	1.1	3	5	1.2	0.0	0.04
Background fraction	0.1	0.4	2	1	0.4	0.4	0.00
Event selection	0.6	1.6	1	14	0.3	0.8	0.08
Fit bias	0.3	0.7	4	8	0.7	1.4	0.02
PID efficiency	0.0	0.1	0	0	0.0	0.1	0.01
Total systematic error	1.2	2.1	5	17	1.5	1.7	0.09
Fit models	1.3	0.7	15	40	1.5	17.2	0.07
r constant	1.4	1.9	12	21	3.8	7.8	0.17
Total model-dependent error	1.9	2.0	19	45	4.1	18.9	0.18

VII. SUMMARY

In conclusion, we measure the total branching fraction of the $B^- \to D^+\pi^-\pi^-$ decay to be

$$\mathcal{B}(B^- \to D^+\pi^-\pi^-) = (1.08 \pm 0.03 \pm 0.05) \times 10^{-3},$$

where the first error is statistical and the second is systematic.

Analysis of the $B^- \to D^+\pi^-\pi^-$ Dalitz plot using the isobar model confirms the existence of a narrow D_2^{*0} and a broad D_0^{*0} resonance as predicted by heavy quark effective theory. The mass and width of D_2^{*0} are determined to be

$$m_{D_2^{*0}} = (2460.4 \pm 1.2 \pm 1.2 \pm 1.9) \text{ MeV}/c^2 \quad \text{and}$$

$$\Gamma_{D_2^{*0}} = (41.8 \pm 2.5 \pm 2.1 \pm 2.0) \text{ MeV},$$

respectively, while for the D_0^{*0} they are

$$m_{D_0^{*0}} = (2297 \pm 8 \pm 5 \pm 19) \text{ MeV}/c^2 \quad \text{and}$$

$$\Gamma_{D_0^{*0}} = (273 \pm 12 \pm 17 \pm 45) \text{ MeV},$$

where the first and second errors reflect the statistical and systematic uncertainties, respectively, the third one is the uncertainty related to the assumed composition of signal events and the Blatt-Weisskopf barrier factors. The measured masses and widths of both states are consistent with the world averages [5] and the predictions of some theoretical models [39–41].

We have also obtained exclusive branching fractions for D_2^{*0} and D_0^{*0} production:

$$\mathcal{B}(B^- \to D_2^{*0}\pi^-) \times \mathcal{B}(D_2^{*0} \to D^+\pi^-)$$
$$= (3.5 \pm 0.2 \pm 0.2 \pm 0.4) \times 10^{-4}$$

and

$$\mathcal{B}(B^- \to D_0^{*0}\pi^-) \times \mathcal{B}(D_0^{*0} \to D^+\pi^-)$$
$$= (6.8 \pm 0.3 \pm 0.4 \pm 2.0) \times 10^{-4}.$$

Our results for the masses, widths, and branching fractions are consistent with but more precise than previous measurements performed by Belle [12].

The relative phase of the scalar and tensor amplitude is measured to be

$$\phi_{D_0^{*0}} = -2.07 \pm 0.06 \pm 0.09 \pm 0.18 \text{ rad}.$$

ACKNOWLEDGMENTS

[1] N. Isgur and M. B. Wise, Phys. Lett. B **232**, 113 (1989).
[2] M. Neubert, Phys. Rep. **245**, 259 (1994).
[3] A. F. Falk and M. Luke, Phys. Lett. B **292**, 119 (1992).
[4] A. F. Falk and M. E. Peskin, Phys. Rev. D **49**, 3320 (1994).
[5] C. Amsler *et al.* (Particle Data Group), Phys. Lett. B **667**, 1 (2008).
[6] H. Albrecht *et al.* (ARGUS Collaboration), Phys. Lett. B **232**, 398 (1989).
[7] J. C. Anjos *et al.* (Tagged Photon Spectrometer Collaboration), Phys. Rev. Lett. **62**, 1717 (1989).
[8] P. Avery *et al.* (CLEO Collaboration), Phys. Rev. D **41**, 774 (1990).
[9] T. Bergfeld *et al.* (CLEO Collaboration), Phys. Lett. B **340**, 194 (1994).
[10] P. L. Frabetti *et al.* (E687 Collaboration), Phys. Rev. Lett. **72**, 324 (1994).
[11] P. Avery *et al.* (CLEO Collaboration), Phys. Lett. B **331**, 236 (1994).
[12] K. Abe *et al.* (Belle Collaboration), Phys. Rev. D **69**, 112002 (2004).
[13] J. M. Link *et al.* (FOCUS Collaboration), Phys. Lett. B **586**, 11 (2004).
[14] K. Abe *et al.* (Belle Collaboration), Phys. Rev. Lett. **94**, 221805 (2005).
[15] A. Abulencia *et al.* (CDF Collaboration), Phys. Rev. D **73**, 051104 (2006).
[16] A. Kuzmin *et al.* (Belle Collaboration), Phys. Rev. D **76**, 012006 (2007).
[17] D. Buskulic *et al.* (ALEPH Collaboration), Z. Phys. C **73**, 601 (1997).
[18] A. Anastassov *et al.* (CLEO Collaboration), Phys. Rev. Lett. **80**, 4127 (1998).
[19] V. M. Abazov *et al.* (D0 Collaboration), Phys. Rev. Lett. **95**, 171803 (2005).
[20] J. Abdallah *et al.* (DELPHI Collaboration), Eur. Phys. J. C **45**, 35 (2006).
[21] B. Aubert *et al.* (*BABAR* Collaboration), Phys. Rev. D **76**, 051101 (2007).
[22] D. Liventsev *et al.* (Belle Collaboration), Phys. Rev. D **77**, 091503 (2008).
[23] B. Aubert *et al.* (*BABAR* Collaboration), arXiv:0808.0333 [Phys. Rev. Lett. (to be published)].
[24] B. Aubert *et al.* (*BABAR* Collaboration), Phys. Rev. Lett. **101**, 261802 (2008).
[25] M. Kobayashi and T. Maskawa, Prog. Theor. Phys. **49**, 652 (1973).
[26] Charged conjugate states are implied throughout the paper.
[27] S. Agostinelli *et al.* (GEANT4 Collaboration), Nucl. Instrum. Methods Phys. Res., Sect. A **506**, 250 (2003).
[28] D. J. Lange, Nucl. Instrum. Methods Phys. Res., Sect. A **462**, 152 (2001).
[29] T. Sjöstrand, Comput. Phys. Commun. **82**, 74 (1994).
[30] B. Aubert *et al.* (*BABAR* Collaboration), Nucl. Instrum. Methods Phys. Res., Sect. A **479**, 1 (2002).
[31] G. C. Fox and S. Wolfram, Phys. Rev. Lett. **41**, 1581 (1978).
[32] H. Albrecht *et al.* (ARGUS Collaboration), Z. Phys. C **48**, 543 (1990).
[33] J. Blatt and V. Weisskopf, *Theoretical Nuclear Physics* (John Wiley & Sons, New York, 1952), p. 361.
[34] C. Zemach, Phys. Rev. **140**, B97 (1965).
[35] E. Barberio and Z. Was, Comput. Phys. Commun. **79**, 291 (1994).
[36] S. Dobbs *et al.* (CLEO Collaboration), Phys. Rev. D **76**, 112001 (2007).
[37] 0.04% is the probability to obtain a χ^2 of 182 or greater for a collection of 153 standard normal-distributed numbers, of which the four largest positive deviations have been removed.
[38] D. V. Bugg, J. Phys. G **36**, 075003 (2009).
[39] N. Isgur, Phys. Rev. D **57**, 4041 (1998).
[40] D. Ebert, V. O. Galkin, and R. N. Faustov, Phys. Rev. D **57**, 5663 (1998).
[41] Y. S. Kalashnikova and A. V. Nefediev, Phys. Lett. B **530**, 117 (2002).